Mid- to Far- Infrared Sensing: $SrTiO_3$, a Novel Optical Material.

N. Kalfagiannis, *[a] J. L. Stoner, [b] J. Hillier, [a] I. Vangelidis, [c] and E. Lidorikis [c]

Polar dielectric crystals have been proposed as a disruptive technological solution to the inflated expectations of plasmonics. The excitation of low-loss surface-phonon polaritons and localized surface-phonon resonances throughout the IR spectrum gives rise to new opportunities, otherwise unachievable due to the inherent losses of metal-based plasmonics. In this work we present, for the first time, the exciting capabilities of $SrTiO_3$, an important technological material that has been overlooked as an active element for nano-photonics.

Introduction

Plasmonics is a research field promising radical breakthroughs in a variety of technological areas,[1] such as photodetection, photocatalysis, biosensing and solar harvesting, to name a few. It deals with the excitation of collective charge oscillations (either electrons or holes) at conductive nanostructures giving rise to resonant optical nanoscale phenomena, which result in extreme subwavelength focusing and enhanced light-matter interactions. However, the plethora of expectations has also been hit by some practical roadblocks causing many plasmonic applications to be still lagging behind. The main fundamental limitations are associated with optical losses and spectral restrictions. In response to this challenge, the scientific community is seeking for solutions that on the one hand combine the novel optical properties of materials with intrinsic or extrinsic mechanisms to attenuate optical losses and on the other hand expand their operation to unexplored spectral ranges, such as the infrared and THz. These wavelengths offer a plethora of applications, for example, the mid-infrared (mid-IR) range is considered the molecular fingerprint region where the fundamental molecular vibrations of biochemical building blocks such as proteins, lipids and DNA are manifested.[2] However, the optical signal of those elements is extremely weak and plasmonic materials are excellent candidates to enhance their detection. In addition, blackbody emission peaks in this spectral range, making it a point of interest for IR sources, imagers and detectors.[2] Far-infrared (far-IR) and THz wavelengths, on the other hand, become important for photo-thermal detection relevant to molecular rotational transitions, space applications, far-IR sources (which are currently limited, exceptionally bulky and require cryogenic cooling) and security applications (including imaging through opaque objects), to name a few. Towards this direction, it has been viewed that one of the most disruptive technologies will be the "*all dielectric plasmonics*".[3]

This proposal may seem kindly contradicting, since dielectric materials do not have any free carriers to collectively resonate with an external electromagnetic field. But resonant plasmonic effects are not exclusive to free charges. Bound charges, as for example charged ions, can also be considered. In that respect, polar dielectric crystals can be used to couple an external electromagnetic field to collective lattice oscillations, namely optical phonons. Similar to plasmonic materials, polar crystals support optical modes in the infrared that can be confined either to the surface of the material or can be highly confined within or in the vicinity of sub-wavelength geometries, resulting in strong field enhancement. The former is known as Surface Phonon Polaritons (SPhP) and the later as Localised Surface Phonon Resonances (LSPhR).[4] Beyond polar materials, there is also another route that enables the *all dielectric nanophotonic* technology; employing high-index dielectric nanoparticles[5,6] that support optically-induced electric and magnetic Mie resonances, as identified by G. Mie,[7] in the early 1900s. In this work, we focus our attention to the former approach, that of polar dielectric crystals.

The elementary theory behind plasmonic excitations is macroscopic,[8] and so similarly to their metallic counterparts, these oscillations can only be supported when the real permittivity is negative. In the case of the polar dielectrics this happens at the so-called Reststrahlen band, the spectral range between the transverse and longitudinal optical phonons. Naturally, the extent of the Reststrahlen band is of great importance as it defines the spectral range for which a polar dielectric can support both LSPhRs at nanostructures and propagating SPhPs at planar surfaces. Interestingly, optical phonons can exhibit larger lifetimes than free carriers and thus, typically, optical losses of phononic materials can be significantly lower than their plasmonic counterparts (bulk optical phonon lifetimes reside in the ps regime in contrast to their electron counterparts which are order of magnitudes smaller).[2] As a result, higher quality factors may be realised with LSPhRs.[2,9,10]

The potential of LSPhR resonant particles has been first demonstrated by Hackwell[11] and Treffers & Cohen,[12] back in the 1970's, reporting a relatively broad resonance peak from interstellar SiC particles and later by Anderson[9], who presented the applicability of SiC and Al_2O_3 nanoparticles for surface enhanced infrared absorption. Recently, Feng et al.[4] demonstrated LSPhRs supported by GaN nanostructures. Efforts focusing on the use of SPhP materials for realizing localized resonances were envisioned also by Hillenbrand *et al.*[10] demonstrating the strong enhancement of optical near-field coupling in SiC, while Greffet *et al.*[13] demonstrated that by introducing a periodic microstructure into a polar material, such as SiC, a thermal infrared source can be fabricated that is coherent over large distances and radiates in well-defined directions. More recently, the realization of two-dimensional van der Waal's crystals, such as hexagonal boron nitride (*h*-BN) opened even more opportunities in nano-photonics.[14–17]

All SPhP phenomena occur within the Reststrahlen range, and thus the bulk optical response of the polar dielectric crystals is of great importance. In Fig. 1 the real and imaginary permittivity of the most prominent polar dielectric crystals is shown, retrieved from the literature (Sapphire,[18] GaN,[19] GaP,[19] *h*-BN,[15] SiC,[20] Al_2O_3,[21] ZnO,[22] GaAs,[19] InP,[19]). Figure 1 also presents the dielectric function of a $SrTiO_3$ (100) crystal (thick solid red lines),

measured in-house with an Infrared Variable Angle Spectroscopic Ellipsometry (Woollam IR-VASE, Mark II).

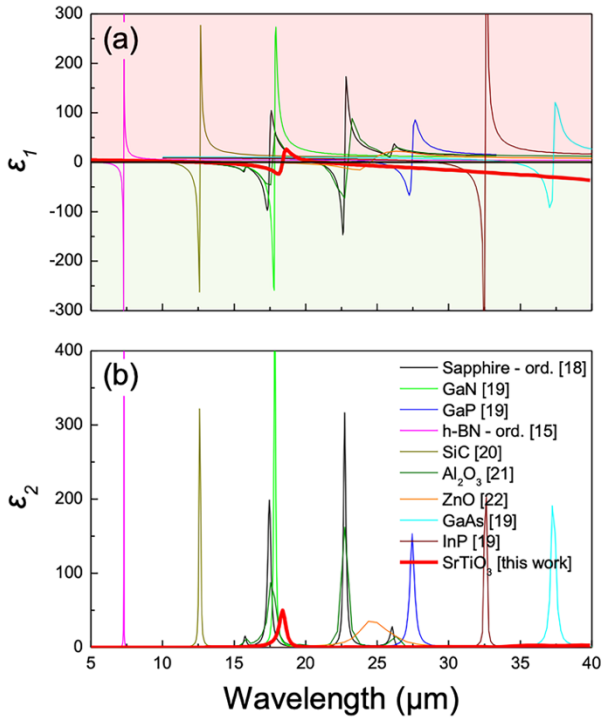

Fig. 1 Comparison of the (a) real, ε_1, and (b) imaginary, ε_2, dielectric permittivity of the most prominent dielectric crystals examined for supporting SPhPs. Literature data are compared with the dielectric permittivity of $SrTiO_3$ (red thick solid line), whose optical constants have been measured with an infrared variable angle spectroscopic ellipsometer. In (a) the green and red shaded areas discriminate between the areas where $\varepsilon_1<0$ and $\varepsilon_1>0$, respectively.

$SrTiO_3$ (STO) is a key technological dielectric material (transparent to visible light, with a band gap of 3.22 eV) of the perovskite family. It has been investigated for many years due to its excellent dielectric, piezoelectric, ferroelectric and optoelectronic properties.[23–25] When a small number of electrons are introduced in the lattice (e.g. in oxygen deficient STO, doped with metals, such as Fe[26,27] or Nb[26,28] or as in the case of reduced STO[29]) many other attractive properties arise such as superconductivity, ferromagnetism, high thermoelectric coefficient, blue and green light emission as well as accommodation of a two dimensional electron gas.[25,30]

However, although its optical constants are known for a while,[24,25] STO has not received great attention as a potential polar dielectric core component for nano-photonic applications. Although Zhnog *et al.*[31] have included STO in their survey for possible mid-IR materials and Kehr *et al.*[32] suggest STO as a component for a negative index material, working as a superlens with sub-diffraction resolution, in both cases their measurement is restricted in a short spectral range (10 – 20 μm) missing out an important part of the far-IR spectrum and thus the further chances of STO to become a viable solution towards longer wavelengths. In this work we critically explore the dielectric function of STO and demonstrate, by comparison, that it exhibits a unique feature which yields additional advantages and flexibility in the design of new infrared components. This may throw STO directly into centre stage for future infrared nanophotonic applications.

Results and discussion

Spectroscopic Ellipsometry

The unique feature of STO is demonstrated in Fig. 2, where we present the real and imaginary permittivity measured by FT-IR synchrotron ellipsometry[25] (dashed lines) and our IR-VASE (solid lines).

The line shape is due to a unique combination of phonon-related properties:

(i) ε_1 becomes negative in the range between the transverse oxygen-related optical mode at 542 cm^{-1} (18.45 microns) and the longitudinal oxygen-related mode at 792 cm^{-1} (12.62 microns – point where $\varepsilon_1=0$), which is the definition of the Reststrahlen band.

(ii) uniquely in STO, a second and very extended range emerges where $\varepsilon_1<0$. This extends between the very strong Sr-related transverse optical phonon (TO_{Sr}), located at ~87 cm^{-1} (114.9 μm) and the longitudinal titanium-related optical phonon (LO_{Ti}) located at 472 cm^{-1} (21.19 μm). Such an effective overlap of two Reststrahlen bands (i.e. the Sr-related TO_{Sr}-LO_{Sr} and Ti-related TO_{Ti}-LO_{Ti}) is not typical to ionic crystals (see Fig. 1a) and is manifested here by the remarkably strong TO_{Sr} phonon.

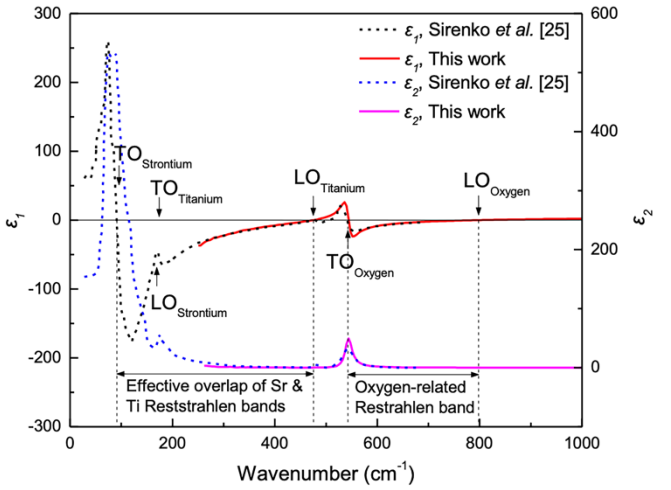

Fig. 2 Real and imaginary permittivity measured by synchrotron radiation[25] (black and blue dashed lines respectively) and by IR-VASE (red and magenta solid lines respectively). The optical phonon modes are noted by arrows.

Propagating Surface Phonon Polaritons

This overlooked optical property of STO provides excellent opportunities for LSPhRs and propagating SPhP modes that can be supported in nanostructures and on surfaces of STO with remarkable tunability (up to ~3 THz). Additionally, the small negative values of ε_1 are accompanied with extremely low ε_2 values which remain low for our measured range (250 cm^{-1} – 8000 cm^{-1}), an indication of low-loss opportunities. Figure 3 demonstrates this capability by presenting the dispersion relationship of phonon polariton modes of STO in air and Si, based on the equation:[8]

$$\hbar k_{||} c = \hbar\omega \cdot Re\left(\sqrt{\frac{\tilde{\varepsilon}_{STO}\cdot\tilde{\varepsilon}_{D}}{\tilde{\varepsilon}_{STO}+\tilde{\varepsilon}_{D}}}\right) \quad (1)$$

Two surface phonon polariton-like solutions appear, one in each respective Reststrahlen ($\omega_{TO} < \omega < \omega_{LO}$) band where $\varepsilon_1(\omega)<0$, *i.e.* in between the O-related modes and in between

the combined Ti-Sr related modes.[24,25] The SPhP solutions are represented by green solid lines in Fig. 3a while the blue solid lines represent the radiative phonon polariton (RPhP) modes. Another important immediate consequence of STO's optical constants is that the total reflection spectral range ("A" areas in Fig. 3b) is extended towards the lower photon energies, making STO a "perfect" reflector for a wide range of wavelengths.

SPhPs at two interfaces, STO/air and STO/Si, are shown in Fig. 3a. In the former case the modes are closer to the light cone, with the high energy branch exhibiting a larger bandwidth of high localization and low group velocity (spectral range where $k_{||} \gg \omega/c$ with group velocity $v_G = d\omega/dk$) compared to the low energy branch. In the STO/Si case, however, the SPhP of the low energy branch exhibits a remarkably large bandwidth of high localization and low group velocity ($k_{||} \gg n_{Si}\omega/c$ spectral range). This is facilitated by the very large Reststrahlen zone, as can be appreciated by the plot of Fig. 3a.

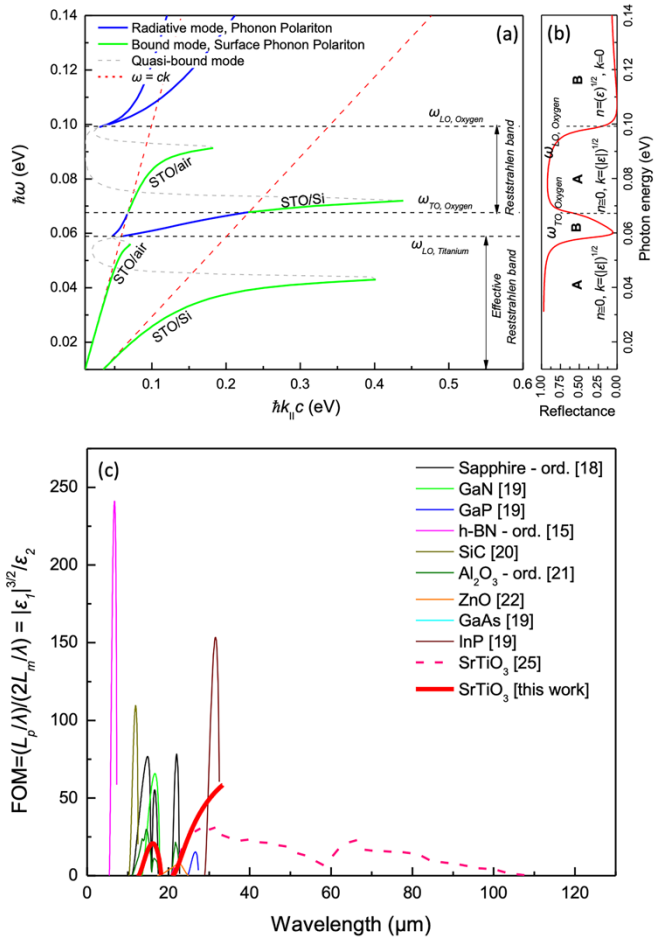

Fig. 3 (a) SPhP dispersion relation at STO/Air and STO/Si interface. (b) Reflectance of STO, calculated by its optical constants (n, k) at normal incidence. (c) Comparison of calculated propagating polariton FOM for all the materials shown in Fig. 1.

A large bandwidth for SPhPs can be instrumental for easy broadband coupling into slow and highly-localized guided modes. Adding to this the existence of two SPhP branches makes STO a truly unique broadband material for IR sensing applications.

We finish this section by providing an example of the propagation length and the confinement in the dielectric employing a Figure of Merit (FOM) that represents the ratio of the propagation length L_p to the vertical extent L_m (field confinement orthogonal to propagation direction). We follow the formalism presented by Caldwell *et al.*[2] according to the equation:

$$\mathrm{FOM} = \frac{L_p/\lambda}{2L_m/\lambda} = \frac{|\varepsilon_1(\omega)|^{3/2}}{\varepsilon_2(\omega)} \qquad (2)$$

Using the above theoretical treatment, we calculate the FOM for the polar dielectrics shown in Fig. 1, which we demonstrate in Fig. 3c. Most of the materials can provide significant advantages for propagating modes with higher FOMs albeit at very restricted spectral ranges. STO on the contrary shows a remarkable capability to demonstrate comparable performance in extended spectral ranges, up to 100 μm, presenting a significant advantage for becoming a single material platform across a significant part of the IR spectrum.

Localised Surface Phonon Resonances

Evidently, STO may offer remarkable opportunities for LSPhRs as well, which we elucidate employing finite-difference time-domain calculations. Two-dimensional projections (cross-section and top view) of the three-dimensional simulation cell are shown in Fig. 4a. Perfectly matched layer (PML) absorbing boundary conditions are applied along the propagation direction, while periodic boundary conditions (PBC) are applied in the lateral directions.

The remarkable capability of STO to tailor its LSPhRs across a wide spectral range is illustrated in Fig. 4b where we present a colour-coded absorption map of STO disks (400 nm in diameter, 200 nm in thickness) as a function of the refractive index of the substrate on which they reside.

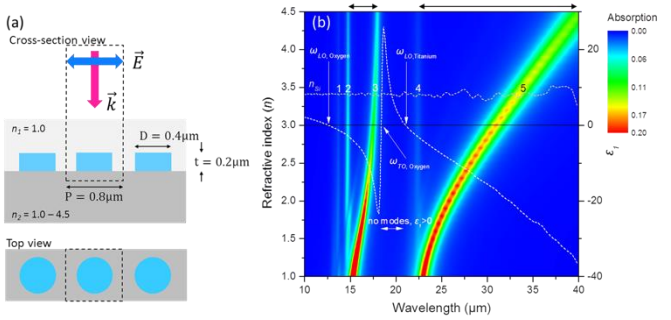

Fig. 4 (a) Schematic illustration of the cross-sectional and top view simulation set-up and geometry of the STO disks. The disk thickness (t) is 200 nm. The diameter (D) is 400 nm and the pitch (P) is 800 nm. The unit cell of the periodic structure is indicated by the dashed line. The broadband light source is placed above the plasmonic structure at normal incidence. (b) Global absorption map of STO nanostructures on various substrates. Within the graph, the IR ellipsometric measurements of STO's real permittivity (white dashed line) and Si's refractive index (grey short dashed line) are superimposed. The main normal phonon modes of the bulk STO are shown with white arrows. Numbers 1 – 5 indicate the location of the absorption peaks of the LSPhRs.

The real part of STO's dielectric function is super-positioned in the same graph (white dashed line) to uncover the physical mechanism contributing to the various localized modes. The demonstrated red-shift is remarkable for a polar crystal. In materials with phonon modes at similar wavelengths the LSPhRs are very localised at the vicinity of the TO mode (a comparison between STO, Sapphire, GaN and GaP is shown in the electronic supplementary information) making STO an unparalleled material of choice for mid-IR to far-IR applications. Of course, varying the refractive index of the substrate is not the only possibility to tailor the LSPhRs of STO resonators. LSPhRs can be excited by an extreme variety of particle sizes

which can extend to several microns (electronic supplementary information), rendering this material compatible with simple lithographic techniques (*i.e.* less sophisticated and time consuming than UV photolithography or e-beam lithography).

In Fig. 4b we observe 3 modes bound at 13.8 μm (1), 14.8 μm (2) and 22.5 μm (4), which emerge as sharp lines across the different substrates. These modes can be accounted to LSPhRs that become resonant at the top of the disks and thus are always screened by Air irrespective of the substrate index. The other two modes (3) and (5), on the other hand, start at the spectral position of modes (2) and (4) respectively, but are red-shifted with increasing substrate index. These can be attributed to LSPhR modes that become resonant in the vicinity of the substrate, and thus undergo increased screening resulting in redshift. The shorter wavelength mode (3) is sharp and redshifts across the oxygen Reststrahlen band. This red-shift is restricted to the $\omega_{TO,\text{Oxygen}}$ limit, upon which the real permittivity becomes positive again.

The $\varepsilon_1(\omega) < 0$ condition (shown with the black arrows above the graph) is satisfied, again, above the $\omega_{LO,\text{ Titanium}}$ and as a result the longer wavelength mode (5) redshifts up to 40 μm. Evidently, STO exhibits a distinct capability in tailoring its LSPhRs across a wide spectral range. Importantly, it presents a multi-resonant behaviour with an elementary, uncomplicated structure which can be of importance in label-free and chemically specific photonic biosensor in multi-analyte chemical or biological systems.[33]

To elucidate the nature of the localised modes the spatial distribution of the E-field intensity enhancement, is plotted on a vertical cross-section at the middle of the disk (Fig. 5a-e) and on a horizontal cross-section at the top (Fig. 5f-j) and the bottom (Fig. 5k-o) of the disk. We choose to calculate the intensity enhancement for nanostructures on top of a Si substrate (n = 3.4, which is shown with grey dashed line in Fig. 4b and measured with our IR VASE). The reason is that Si has been the substrate of choice for epitaxial growth of STO thin films.[34–37] Interestingly, STO/Si heterojunctions have shown pyroelectric properties near room temperature.[38]

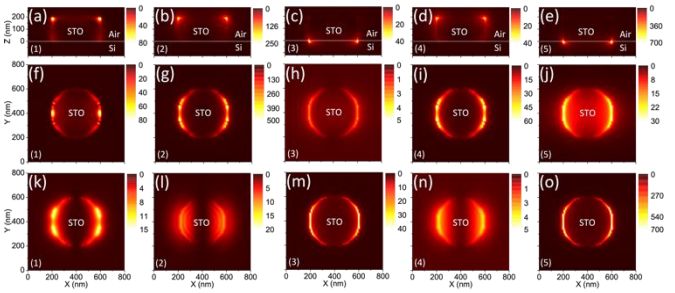

Fig. 5 (a-e) E-field intensity enhancement, plotted on a vertical cross section (middle of the disk) at the peak absorption wavelengths, 1-5 shown in Fig. 3b. (f-j) E-field intensity enhancement, plotted on a horizontal cross section at the top of the disk. (k-o) E-field intensity enhancement, plotted on a horizontal cross section at the bottom of the disk.

Figure 5 reveals the underlying nature of all resonant modes: modes 3 and 5 are the standard dipole Fröhlich modes in the proximity of the substrate, modes 2 and 4 are standard dipole Fröhlich modes in the top of the disk and thus in proximity of air, while mode 1 is a higher order mode (quadrupole) localised mainly at the interface with the air environment. Evidently, the highest intensity enhancement is observed at the longer wavelength mode.

Evidence of strong coupling

As a last section, we theoretically demonstrate far-IR strong coupling phenomena between STO LSPhR and a molecular excitation state. This highlights the possibility of using STO photonic resonators in a variety of new generation opto-electronic devices such as surface enhanced infrared absorption (SEIRA) and mid-IR light sources. Several experimental and theoretical studies[14,39–43] have shown the emergence of this regime, in a variety of systems. The strong coupling phenomenon can be approached either classically (system composed of coupled oscillators) or quantum mechanically (exchange of an elementary quantum of energy).[43,44]

In particular, the sensing capability of the disk-shaped antennas was explored by calculating the reflectance, transmission and absorption spectra of the STO antennas on top of Si (shown in the electronic supplementary information), covered by a thin molecular film (100 nm). Optically, the molecular thin film is described by a Lorentzian line shape, with its central wavelength varied so to scan the entire range between 30 – 40 μm, where the strongest dipole moment of the antennas is located (Fig. 4b mode 5). The global picture of interaction between the molecular thin film and the STO LSPhR is demonstrated in Fig. 6. The red dashed line represents the excitonic response of the molecule across the entire wavelength range of interest while the black dashed line is characteristic of the LSPhR of the STO antennas.

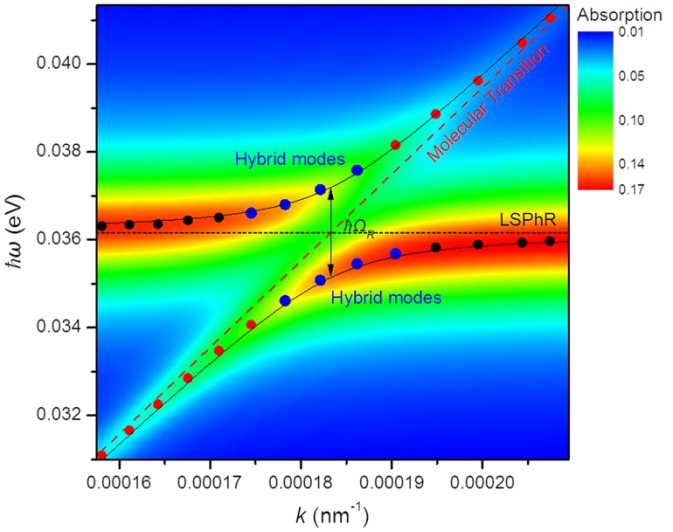

Fig. 6 Global absorption map of 100 nm molecular thin film on top of the STO nano-antennas. The wavenumber k of the molecular transition is varied so to scan from 30 μm to 40 μm (step of 150 nm) while unvarying γ_{mol} and σ_{mol}. The red dashed line represents the response of the molecule as we scan its absorption frequency while the black dashed line renders the LSPhR of the STO antennas. The black and red circles illustrate the peak position of the LSPhRs and the molecular excitation respectively. The blue dots illustrate the hybrid modes. Employing Eq. (3) we fit the FDTD data, using g as the adjustable parameter. The thin black solid lines represent the best fitted curve. The pronounced anti-crossing suggests a strong coupling between the LSPhR modes and the thin film resonance.

The plot of Fig. 6 colour-codes the total absorption of the hybrid system. The colour-coded maps of reflectance and transmittance follow the same pattern and, as expected, are colour reciprocal to each other (shown in Fig. S8 of the electronic supplementary information). We note the modification of the LSPhR peak as it crosses with the thin film

absorption peak. The total absorption of the hybrid system enhances the bare molecular absorption (shown in the electronic supplementary information) by two orders of magnitude, yielding the STO photonic resonators as promising candidates for SEIRA.

The black and red circles illustrate the peak position of the LSPhRs and the molecular excitations respectively, while the blue dots illustrate the hybrid modes. This pronounced anti-crossing is due to the interaction between the LSPhR modes and the thin film resonance and can be described by the following equation:[14]

$$\omega_{\pm} = \frac{1}{2}(\omega_{LSPhR} + \omega_{mol}) \pm \frac{1}{2} Re\left[\sqrt{4|g|^2 + \left[\delta + i(\frac{\gamma_{mol}}{2} - \frac{\gamma_{LSPhR}}{2})\right]^2}\right] \quad (3)$$

where, ω_{LSPhR}, ω_{mol}, γ_{LSPhR}, and γ_{mol} are the frequencies and damping factors of the LSPhR and molecule respectively, $\delta=\omega_{LSPhR} - \omega_{mol}$ is the detuning between the LSPhR and molecular excitations and g is the coupling strength constant, while $\omega_{\pm}$ are the corresponding eigenfrequencies of the coupled system.[44] The signature of this coupling effect (known as Rabi splitting[39,40,42,43,45]) is the emergence of upper and lower branches separated by a characteristic energy, defined as the Rabi energy splitting $\hbar\Omega_R$ when $\delta=0$. Usually, the definition of strong coupling is context sensitive,[43] however, in our case we define strong coupling in the more pragmatic way that the Rabi split is significantly observable (the coupling exceeds the linewidths of the coupled system). Fitting our data (black, red and blue dots of Fig. 6) with Eq. (3) yields a coupling strength g=1.05 meV ($\hbar\Omega_R \sim 2g$), implying that the Rabi energy, $\hbar\Omega_R$, is significantly larger than the widths γ_{LSPhR}, and γ_{mol} and thus coupling dominates over dissipative processes. This condition is required to preserve the quantum coherence.[44] Our FDTD calculations suggest that strong coupling, in principle, can exist between STO localised photonic modes and molecular transitions in the mid- to far-IR range. Those findings may be useful in the efficient design of far-IR lasing or in the design of room temperature far-IR photodetectors.[46,47]

Conclusions

To conclude, we have made a first effort to report the promising optical response of STO photonic resonators which show remarkable tunability from mid to far infrared wavelengths. At first, we examined its bulk dielectric function and compared it with the most prominent polar dielectric crystals. By inspection, we were able to identify that, fundamentally, the range of operation of STO is extending to wider wavelength ranges. Importantly, its real permittivity naturally allows for localised surface phonon resonances (LSPhRs) to be achieved for a wide range of particle sizes (up to several microns) allowing the adaptation of simple nanostructuring techniques.

We then utilised the measured dielectric function within the Finite-Difference Time-Domain framework and performed calculations on a specific antenna geometry. We demonstrate some interesting phenomena arising from the bulk optical properties and we report that certain modes can be tuned up to the far-IR regime. The LSPhR modes observed were classified and analysed. Finally, we demonstrated the strong coupling between a STO photonic resonator and a molecular thin film to illustrate its capabilities for surface enhanced infrared absorption. Overall, STO is an exemplary material for many important technological applications and this work establishes a further pathway, unexplored so far; that of nano-photonics in the mid- and far- IR regimes.

Conflicts of interest

There are no conflicts to declare.

Acknowledgements

The authors would like to acknowledge the supply of the STO single crystal from Prof. Matthew J Rosseinsky supported by the EPSRC grant EP/N004884/1.

References

1 H. A. Atwater, *ACM SIGDA Newsl.*, 2007, **37**, 1–1.
2 J. D. Caldwell, L. Lindsay, V. Giannini, I. Vurgaftman, T. L. Reinecke, S. A. Maier and O. J. Glembocki, *Nanophotonics*, , DOI:10.1515/nanoph-2014-0003.
3 Editorial, *Nat. Nanotechnol.*, 2016, **11**, 1–1.
4 K. Feng, W. Streyer, S. M. Islam, J. Verma, D. Jena, D. Wasserman and A. J. Hoffman, *Appl. Phys. Lett.*, 2015, **107**, 081108.
5 A. Krasnok, R. Savelev, D. Baranov and P. Belov, in *World Scientific Handbook of Metamaterials and Plasmonics*, World Scientific, 2017, pp. 337–385.
6 S. Jahani and Z. Jacob, *Nat. Nanotechnol.*, 2016, **11**, 23.
7 G. Mie, *Ann. Phys.*, 1908, **330**, 377–445.
8 S. A. Maier, *Plasmonics: Fundamentals and Applications*, Springer US, New York, NY, 2007.
9 M. S. Anderson, *Appl. Phys. Lett.*, 2003, **83**, 2964–2966.
10 R. Hillenbrand, T. Taubner and F. Keilmann, *Nature*, 2002, **418**, 159–162.
11 J. A. Hackwell, *Astron. Astrophys. Vol. 21, p. 239*, 1972, **21**, 239.
12 R. Treffers and M. Cohen, *Astrophys. J.*, 1974, **188**, 545.
13 J.-J. Greffet, R. Carminati, K. Joulain, J.-P. Mulet, S. Mainguy and Y. Chen, *Nature*, 2002, **416**, 61–64.
14 M. Autore, P. Li, I. Dolado, F. J. Alfaro-Mozaz, R. Esteban, A. Atxabal, F. Casanova, L. E. Hueso, P. Alonso-González, J. Aizpurua, A. Y. Nikitin, S. Vélez and R. Hillenbrand, *Light Sci. Appl.*, 2018, **7**, 17172.
15 A. J. Giles, S. Dai, I. Vurgaftman, T. Hoffman, S. Liu, L. Lindsay, C. T. Ellis, N. Assefa, I. Chatzakis, T. L. Reinecke, J. G. Tischler, M. M. Fogler, J. H. Edgar, D. N. Basov and J. D. Caldwell, *Nat. Mater.*, 2017, **17**, 134–139.
16 S. Dai, Z. Fei, Q. Ma, A. S. Rodin, M. Wagner, A. S. McLeod, M. K. Liu, W. Gannett, W. Regan, K. Watanabe, T. Taniguchi, M. Thiemens, G. Dominguez, A. H. C. Neto, A. Zettl, F. Keilmann, P. Jarillo-Herrero, M. M. Fogler and D. N. Basov, *Science (80-.).*, 2014, **343**, 1125–1129.
17 W. Ma, P. Alonso-González, S. Li, A. Y. Nikitin, J. Yuan, J. Martín-Sánchez, J. Taboada-Gutiérrez, I. Amenabar, P. Li, S. Vélez, C. Tollan, Z. Dai, Y. Zhang, S. Sriram, K. Kalantar-Zadeh, S.-T. Lee, R. Hillenbrand and Q. Bao, *Nature*, 2018, **562**, 557–562.

18 M. Schubert, T. E. Tiwald and C. M. Herzinger, *Phys. Rev. B*, 2000, **61**, 8187–8201.

19 J. A. Woollam Co. Ellipsometry database (WVASE software), 2018.

20 E. D. Palik, *Handbook of Optical Constants of Solids*, Academic Press, 1998.

21 J. Kischkat, S. Peters, B. Gruska, M. Semtsiv, M. Chashnikova, M. Klinkmüller, O. Fedosenko, S. Machulik, A. Aleksandrova, G. Monastyrskyi, Y. Flores and W. Ted Masselink, *Appl. Opt.*, 2012, **51**, 6789.

22 M. R. Querry, *Optical Constants*, 1985.

23 J. H. Haeni, P. Irvin, W. Chang, R. Uecker, P. Reiche, Y. L. Li, S. Choudhury, W. Tian, M. E. Hawley, B. Craigo, A. K. Tagantsev, X. Q. Pan, S. K. Streiffer, L. Q. Chen, S. W. Kirchoefer, J. Levy and D. G. Schlom, *Nature*, 2004, **430**, 758–761.

24 S. Zollner, A. A. Demkov, R. Liu, P. L. Fejes, R. B. Gregory, P. Alluri, J. A. Curless, Z. Yu, J. Ramdani, R. Droopad, T. E. Tiwald, J. N. Hilfiker and J. A. Woollam, *J. Vac. Sci. Technol. B Microelectron. Nanom. Struct.*, 2000, **18**, 2242.

25 A. A. Sirenko, C. Bernhard, A. Golnik, A. M. Clark, J. Hao, W. Si and X. X. Xi, *Nature*, 2000, **404**, 373–376.

26 S. Taibl, G. Fafilek and J. Fleig, *Nanoscale*, 2016, **8**, 13954–13966.

27 A. S. Kumar, P. Suresh, M. M. Kumar, H. Srikanth, M. L. Post, K. Sahner, R. Moos and S. Srinath, *J. Phys. Conf. Ser.*, 2010, **200**, 092010.

28 C. Z. Bi, J. Y. Ma, J. Yan, X. Fang, B. R. Zhao, D. Z. Yao and X. G. Qiu, *J. Phys. Condens. Matter*, 2006, **18**, 2553–2561.

29 W. S. Baer, *Phys. Rev.*, 1966, **144**, 734–738.

30 X. Hao, Z. Wang, M. Schmid, U. Diebold and C. Franchini, *Phys. Rev. B*, 2015, **91**, 085204.

31 Y. Zhong, S. D. Malagari, T. Hamilton and D. Wasserman, *J. Nanophotonics*, 2015, **9**, 093791.

32 S. C. Kehr, Y. M. Liu, L. W. Martin, P. Yu, M. Gajek, S.-Y. Yang, C.-H. Yang, M. T. Wenzel, R. Jacob, H.-G. von Ribbeck, M. Helm, X. Zhang, L. M. Eng and R. Ramesh, *Nat. Commun.*, 2011, **2**, 249.

33 D. Rodrigo, A. Tittl, N. Ait-Bouziad, A. John-Herpin, O. Limaj, C. Kelly, D. Yoo, N. J. Wittenberg, S.-H. Oh, H. A. Lashuel and H. Altug, *Nat. Commun.*, 2018, **9**, 2160.

34 L. Méchin, G. J. Gerritsma and J. Garcia Lopez, *Phys. C Supercond.*, 1999, **324**, 47–56.

35 X. Hu, H. Li, Y. Liang, Y. Wei, Z. Yu, D. Marshall, J. Edwards, R. Droopad, X. Zhang, A. A. Demkov, K. Moore and J. Kulik, *Appl. Phys. Lett.*, 2003, **82**, 203–205.

36 H. Li, X. Hu, Y. Wei, Z. Yu, X. Zhang, R. Droopad, A. A. Demkov, J. Edwards, K. Moore, W. Ooms, J. Kulik and P. Fejes, *J. Appl. Phys.*, 2003, **93**, 4521–4525.

37 L. V Goncharova, D. G. Starodub, E. Garfunkel, T. Gustafsson, V. Vaithyanathan, J. Lettieri and D. G. Schlom, *J. Appl. Phys.*, 2006, **100**, 14912.

38 G. Bai, D. Wu, Q. Xie, Y. Guo, W. Li, L. Deng and Z. Liu, *J. Adv. Dielectr.*, 2015, **05**, 1550031.

39 J. Sheng, Y. Chao and J. P. Shaffer, *Phys. Rev. Lett.*, 2016, **117**, 103201.

40 H. Wang, A. Toma, H.-Y. Wang, A. Bozzola, E. Miele, A. Haddadpour, G. Veronis, F. De Angelis, L. Wang, Q.-D. Chen, H.-L. Xu, H.-B. Sun and R. P. Zaccaria, *Nanoscale*, 2016, **8**, 13445–13453.

41 R.-Q. Li, F. J. García-Vidal and A. I. Fernández-Domínguez, *ACS Photonics*, 2018, **5**, 177–185.

42 I. G. Savenko, R. G. Polozkov and I. A. Shelykh, *J. Phys. B At. Mol. Opt. Phys.*, 2012, **45**, 045101.

43 P. Törmä and W. L. Barnes, *Reports Prog. Phys.*, 2015, **78**, 013901.

44 B. Kolaric, B. Maes, K. Clays, T. Durt and Y. Caudano, *Adv. Quantum Technol.*, 2018, **1**, 1800001.

45 D. Melnikau, R. Esteban, D. Savateeva, A. Sánchez-Iglesias, M. Grzelczak, M. K. Schmidt, L. M. Liz-Marzán, J. Aizpurua and Y. P. Rakovich, *J. Phys. Chem. Lett.*, 2016, **7**, 354–362.

46 K. Ohtani, M. Beck, M. J. Süess, J. Faist, A. M. Andrews, T. Zederbauer, H. Detz, W. Schrenk and G. Strasser, *ACS Photonics*, 2016, **3**, 2280–2284.

47 S. Castilla, B. Terrés, M. Autore, L. Viti, J. Li, A. Y. Nikitin, I. Vangelidis, K. Watanabe, T. Taniguchi, E. Lidorikis, M. S. Vitiello, R. Hillenbrand, K.-J. Tielrooij and F. H. L. Koppens, *Nano Lett.*, 2019, **19**, 2765–2773.